J. Fluid Mech. (2010), *vol.* 656, *pp.* 147–176.
doi:10.1017/S0022112010001072

An experimental investigation of cloud cavitation about a sphere

P. A. BRANDNER[1]†, G. J. WALKER[2], P. N. NIEKAMP[1] AND B. ANDERSON[3]

[1]Australian Maritime College, University of Tasmania, Launceston, Tasmania 7248, Australia

[2]School of Engineering, University of Tasmania, Hobart, Tasmania 7001, Australia

[3]Maritime Platforms Division, Defence Science and Technology Organisation, Fishermans Bend, Victoria 3032, Australia

(Received 22 July 2009; revised 22 February 2010; accepted 25 February 2010; first published online 21 May 2010)

Cloud cavitation occurrence about a sphere is investigated in a variable-pressure water tunnel using low- and high-speed photography. The model sphere, 0.15 m in diameter, was sting-mounted within a 0.6 m square test section and tested at a constant Reynolds number of 1.5×10^6 with cavitation numbers varying between 0.36 and 1.0. High-speed photographic recordings were made at 6 kHz for several cavitation numbers providing insight into cavity shedding and nucleation physics. Shedding phenomena and frequency content were investigated by means of pixel intensity time series data using wavelet analysis. Instantaneous cavity leading edge location was investigated using image processing and edge detection.

The boundary layer at cavity separation is shown to be laminar for all cavitation numbers, with Kelvin–Helmholtz instability and transition to turbulence in the separated shear layer the main mechanism for cavity breakup and cloud formation at high cavitation numbers. At intermediate cavitation numbers, cavity lengths allow the development of re-entrant jet phenomena, providing a mechanism for shedding of large-scale Kármán-type vortices similar to those for low-mode shedding in single-phase subcritical flow. This shedding mode, which exists at supercritical Reynolds numbers for single-phase flow, is eliminated at low cavitation numbers with the onset of supercavitation.

Complex interactions between the separating laminar boundary layer and the cavity were observed. In all cases the cavity leading edge was structured in laminar cells separated by well-known 'divots'. The initial laminar length and divot density were modulated by the unsteady cavity shedding process. At cavitation numbers where shedding was most energetic, with large portions of leading edge extinction, re-nucleation was seen to be circumferentially periodic and to consist of stretched streak-like bubbles that subsequently became fleck-like. This process appeared to be associated with laminar–turbulent transition of the attached boundary layer. Nucleation occurred periodically in time at these preferred sites and formed the characteristic cavity leading edge structure after sufficient accumulation of vapour had occurred. These observations suggest that three-dimensional instability of the

† Email address for correspondence: P.Brandner@amc.edu.au

decelerating boundary layer flow may have significantly influenced the developing structure of the cavity leading edge.

1. Introduction

Cloud cavitation is a general term for unsteady or periodic cavitation phenomena occurring about a body involving the formation, detachment and collapse of sheet cavities. The collapse or condensation of the shed cavity in the wake of the body forms 'cloud'-like structures. The unsteady nature of cloud cavitation has significant consequences for hydraulic and marine equipment, including problems of unsteady flows, noise, vibration and cavitation erosion. Through the use of modern experimental diagnostics and computational fluid dynamics, significant insights have been gained into the complex physics involved. However, despite these advances there remains much to be understood and cloud cavitation continues to be an active research area.

Most investigation has been directed to cloud cavitation associated with lifting surfaces or hydrofoils, and also internal flows (Brennen 1995; Franc & Michel 2004; Schnerr *et al.* 2006). The occurrence of cloud cavitation in such flows may involve several mechanisms. Brennen (1995) refers to the coherent nature of cloud cavitation as being due to natural instabilities or externally imposed flow fluctuations. Recent reviews by Franc & Michel (2004) and Franc (2001) describe cloud cavitation as originating from either intrinsic or system-based instabilities. Franc & Michel (2004) have investigated and reviewed extensive work on the role of unsteady cavity closure and re-entrant jet formation in cloud cavitation as an intrinsic instability. System-based instabilities are defined as those due to interaction of sheet cavities with the hydraulic circuits of water tunnels or between cavities on neighbouring blades of turbomachinery. The role of surface tension in the generation of cloud cavitation resulting from contact of a re-entrant jet with the boundary of a sheet cavity has been studied by Mørch *et al.* (2003). Shock wave phenomena in cloud cavitation have been also investigated numerically by Reisman, Wang & Brennen (1998) and Schnerr *et al.* (2006).

Cavitation inception and occurrence about axisymmetric bodies, including spheres and various headforms, has been widely studied. Brennen (1970*a*) investigated interfacial phenomena, including boundary layer transition, associated with fully developed or supercavities about various axisymmetric headforms including spheres. In a companion paper, Brennen (1970*b*), described the effects of polymers on interfacial behaviour. Since this early work, interest in cavitation inception and the association of boundary layer separation with cavity formation on spheres and headforms has continued. Arakeri (1975) and Arakeri & Acosta (1973, 1976) reported the dominant influence of viscous effects on cavity formation, particularly the association of liquid surface detachment with laminar boundary layer separation. Reviews and further work on the interaction of cavity formation (or 'detachment' as it is termed by some workers) with boundary layer separation are given in Brennen (1995) and Franc & Michel (2004). More recently, Tassin Leger & Ceccio (1998) and Tassin Leger, Bernal & Ceccio (1998) have reported extensive experimental studies of liquid surface detachment and interfacial phenomena on spheres, headforms and hydrofoils. These workers also investigated the influence of solid/liquid/gas surface energy by testing differing solid materials, both hydrophobic and hydrophilic; cavity interaction with the upstream boundary layer was also studied.

Despite this extensive literature there appears to be little published work on cloud cavitation about bluff bodies. Studies of cavitation about bluff bodies, other than

those discussed above, have focused on inception and coherent phenomena in shear layers associated with bodies having sharp edges or attached cavities on headforms, e.g. those of Arndt (1976), Belahadji, Franc & Michel (1995) and Ceccio & Brennen (1992). A brief outline of the present experimental investigation of cloud cavitation about a sphere has been given by Brandner *et al.* (2007) and preliminary attempts at numerical modelling of this flow have been presented by Schmidt *et al.* (2008).

Practical examples of cloud cavitation about bluff bodies may include ventilated and natural cavity formation about sonar domes and other bluff appendages of surface and undersea vehicles. The present investigation was conceived as a preliminary study to gain basic information on cloud cavitation about bluff bodies and to test experimental methods. Given the extensive work on shedding phenomena for single-phase flow about spheres, this simple body was chosen for initial observations.

Single-phase unsteady flow phenomena in sphere wakes have recently been reviewed by Bakić & Perić (2005). Above $Re \approx 10^3$ (based on diameter and free stream velocity) there are two modes (high and low) of regular vortex shedding. These phenomena have been observed in wind tunnels using hot-wire anemometry and visualization with smoke, and in water tunnels using dye injection assisted by laser light sheet illumination. The low mode, with Strouhal number $St_K \approx 0.2$, corresponds to large-scale Kármán vortex shedding. The large-scale vortices have a horseshoe structure and rotate irregularly around the longitudinal axis of the sphere flow. While local observations may sometimes give the impression of helical vortex structures in the wake, there is no evidence for their existence (which would, in any case, violate Thomson's circulation theorem as discussed by Achenbach 1974).

The high-mode unsteadiness is generated by Kelvin–Helmholtz (K–H) instability in the separating laminar shear layer. The corresponding Strouhal number, St_H, varies as about the 0.7 power of Reynolds number. Bakić & Perić found $St_H = 0.0039Re^{0.695}$ for $22 \times 10^3 < Re < 400 \times 10^3$. There is no evidence for this high-frequency unsteadiness causing discrete vortex shedding behind a sphere.

In the critical regime for single-phase flow ($2 \times 10^5 < Re < 4 \times 10^5$) defined by Achenbach (1972) the unstable separated laminar shear layer undergoes transition to turbulence and reattaches to form a laminar separation bubble; the turbulent boundary layer thus formed subsequently separates at an angle $\phi \approx 120^\circ$ from the forward stagnation point. Above the upper critical Reynolds number ($Re \approx 4 \times 10^5$ with free stream turbulence level about 0.5 %, as in the present investigation) low-mode periodic vortex shedding can no longer be detected in single-phase flow. In the supercritical flow regime ($4 \times 10^5 < Re < 1.5 \times 10^6$ approximately) transition appears to occur in attached flow around $\phi = 95^\circ$, with turbulent separation remaining near $\phi = 120^\circ$. The transcritical flow regime beyond $Re = 1.5 \times 10^6$ is characterized by the location of boundary layer transition progressively moving forward with increasing Reynolds number, until it eventually occurs upstream of the pressure minimum on the sphere.

In cavitating flows the visualization of flow phenomena is facilitated by the presence of the gas/vapour cavities. Vortex structures can easily be identified from the generation of new bubbles within the low-pressure vortex cores, or by the entrainment of bubble clouds into the vortical flow regions. Where large cavities form, it is possible to identify wave phenomena in the shear flow adjacent to the cavity boundary from perturbations of the interfacial surface. K–H instability of the shear layer separating from a cavitating sphere causes transverse flow perturbations that are restrained by surface tension; this produces regular waviness of the interfacial surface that can readily be seen with glancing illumination.

Advances in low- and high-speed digital photography provide significant opportunities for the observation and analysis of unsteady cavitation phenomena.

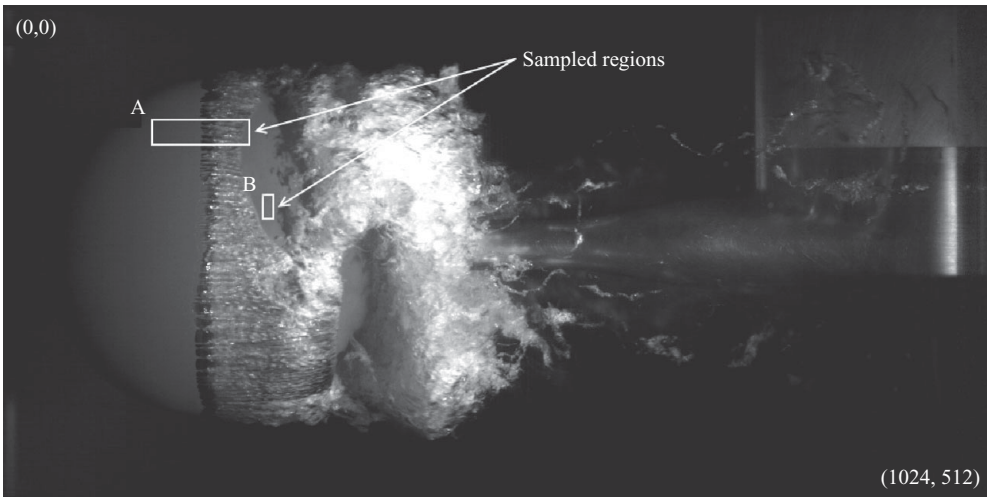

FIGURE 1. Image from high-speed photography of a cavitating sting-mounted sphere located on the test section longitudinal axis (flow from left to right). Sampled regions for leading edge detection (A) and shedding dynamics (B) are indicated. Region A is 100 × 25 pixels centred on the mean leading edge location and vertical pixel 122. Region B is 10 × 25 pixels centred at (275, 210). The time series of the spatial average of the pixel intensity of region B was used for investigating shedding frequency content using wavelet analysis.

In the present investigation these techniques have been used to investigate cloud cavitation about a sphere in a cavitation tunnel. The relatively high spatial resolution of low-speed photography enables small-scale phenomena associated with cavity formation to be discerned. The temporal resolution of the high-speed photography enables the global character and frequency content of the cloud cavitation to be analysed. With suitable lighting the time series data of individual or spatially averaged pixel intensity may be used for frequency analysis. For the present investigation this has been carried out using wavelet analysis. These techniques have been extensively used in the investigation of various turbulent flow phenomena including cloud cavitation (Kjeldsen & Arndt 2001). Reviews of wavelet transform applications have been presented by Farge (1992) and Jaffard, Meyer & Ryan (2001) with practical techniques presented by Torrence & Compo (1998) and Addison (2002).

2. Experimental overview

All tests were performed in the Australian Maritime College's Tom Fink Cavitation Tunnel, a closed recirculating variable-pressure water tunnel. The test section is 0.6 m square × 2.6 m long; the velocity there may be varied from 2 to 12 $\mathrm{m\,s^{-1}}$ and the centreline static pressure from 4 to 400 kPa absolute. Studies may involve the investigation of steady and unsteady flows, two-phase flows including cavitation, turbulence and hydro-acoustics. Details of the tunnel set-up and operation are given in Brandner, Clarke & Walker (2004).

The 0.15 m diameter test sphere was located midway along the test section on the longitudinal axis, supported by a sting mount as shown in figure 1. To minimize weight, the sphere was constructed from PVC in two half-shells mechanically joined and fully coated with 2 pack epoxy (Akso Noble Lesonal 420) to provide a consistent hydraulically smooth surface finish (1200 grit – average particle size 3 μm). This surface was found to be hydrophilic both in the presence of air and the gas content

of natural cavities in subsequent tunnel testing. Testing was carried out at a constant Reynolds number (Re) of 1.5×10^6, which is around the lower limit of the transcritical flow regime in single-phase flow defined by Achenbach (1972). The cavitation number (σ) was varied between 1.0 and 0.36. The Reynolds number is defined as $Re = UD/\nu$ and the cavitation number as $\sigma = (p - p_v)/1/2\rho U^2$, where U is the free stream velocity, D is the sphere diameter, ν is the kinematic viscosity of water, p is the test section static pressure at the sphere centre, p_v is the water vapour pressure and ρ is the water density. Dissolved oxygen content of the tunnel water was maintained at approximately 1.2 p.p.m.

Low-speed (still) photography was carried out using a Canon EOS 300D 35 mm SLR digital camera (3072 × 2048 pixel image resolution) and EF-S 18–55 mm f3.5–5.6 lens with triggered stroboscopic lighting (DRELLO 1018/LE4040). High-speed photography was carried out using a LaVision HighSpeedStar5 camera with a Nikkor 55 mm, f/1.4 lens controlled using DaVis 7.1.3 software, with lighting from a Dedolight DLH650. The camera uses a 10-bit CMOS sensor and was operated at a frame rate of 6 kHz and resolution of 1024 × 512 pixels, with 4096 images recorded for each cavitation number investigated in the range 0.4 to 0.95. Spatial resolution for the low-speed photography was approximately 0.13 mm/pixel and 0.42 mm/pixel for the high-speed photography. With appropriate lighting, the image intensity was found to be useful for identifying various flow features such as cavity leading edge position, nucleation and growth of reforming sheet cavities, laminar–turbulent transition in the interfacial layer, and cavity breakup and cloud formation. A typical image obtained by high-speed photography is shown in figure 1.

Both low- and high-speed photography were used to measure the instantaneous location of the cavity leading edge. Laminar flow over the leading edge of the cavity provided a strong contrast between the scattered light intensity of the cavity surface and the background sphere surface. The instantaneous leading edge location from low-speed photography was taken as the average of upper and lower detachment positions observed on the sphere equator oriented parallel to the tunnel sidewall. Instantaneous leading edge locations from high-speed photography were identified from a region of suitable light intensity and contrast (region A as defined in figure 1). This area of 25 spanwise × 100 streamwise pixels centred on the mean leading edge location and vertical pixel 122, was interrogated for leading edge position using a simple derivative-based edge detection algorithm. A threshold derivative of 32 intensity increments over three streamwise pixels was found to provide reliable results in all cases. The absolute uncertainty in the cavity leading edge angle measured from both low- and high-speed photography is estimated to be $\pm 2.5^\circ$.

For the purposes of quantifying cavity dynamics, time series of pixel intensities within the shedding region were analysed. These were found to have substantial high-frequency noise from fine-scale cavity surface features. An effective means of filtering the time series is spatial averaging within the scale of the structures desired to be resolved. A region of 10 streamwise × 25 spanwise pixels was found to provide sufficient spatial resolution and reduce undesirable noise. For all cavitation numbers tested it was found that a time series resolving all features of interest could be taken from a single region (B, as defined in figure 1) of these dimensions centred at (275, 210). Comparison of time series and statistics obtained from region B shifted upstream and downstream by 10 pixels, and for several spanwise positions between 210 and 310 pixels, showed these data to be essentially independent of the location of the sampled region within these limits. The time series data for each cavitation number were examined using wavelet analysis to investigate the frequency content and coherence of cloud cavitation phenomena. The wavelet analysis method of Torrence & Compo

(1998) was used: a continuous wavelet transformation in Fourier space, employing a DOG (derivative of a Gaussian) order two wavelet.

3. Results

A series of low-speed photographic images of cavitation occurrence about the sphere, for several cavitation numbers, is shown in figure 2. The cavitation may be described to occur in three basic modes summarized and schematically depicted in figure 3. Cavitation inception was observed to appear near $\phi = 97^\circ$ at $\sigma \approx 1.0$, (see figure 10). At this position, the single-phase measurements of Achenbach (1972) indicate a pressure coefficient close to -1.0; this accords with the observation of Arakeri & Acosta (1973, 1976) that for attached flow the value of σ at inception appears to correlate with the negative value of the static pressure coefficient at the transition location. In this case the activation of cavitation nuclei is evidently due to internal stresses associated with the violent turbulent breakdown process. More recent studies do, however, show that a more rigorous criterion for cavitation inception is that based on the total normal stress (Joseph 1998; Padrino *et al.* 2007).

The cavity formed at $\sigma = 1.0$ was stable and of about $0.15D$ in length, as shown in figure 2(*a*). Due to the large range of cavitation numbers investigated, a low dissolved gas content in the circulating water was used to minimize the presence of large bubbles at the lower cavitation numbers. Consequently, some hysteresis was observed at inception due to the lack of nuclei, with a higher 'desinent' cavitation number required to eliminate the sheet cavity after inception.

With reduction of the cavitation number to 0.95 the sheet cavity became unstable, initiating cloud cavitation. Cloud cavitation was observed to occur for $0.95 > \sigma > 0.4$, as shown in figures 2(*b*)–2(*g*). The moderate cavity lengths established over this range of σ values allowed the development of re-entrant jet phenomena; these dominated cavity breakup, resulting in large-scale vortex shedding and bubble cloud formation. For $\sigma < 0.4$, re-entrant jet phenomena no longer promoted large-scale breakup of the cavity, resulting in the supercavitating flow regime seen in figure 2(*h*). Flows where cavity closure occurs well downstream of bluff axisymmetric bodies have been described by Brennen (1995) as fully developed cavitation, but have also been described in the literature as being supercavitation (Van den Braembussche 2002; Franc & Michel 2004). Herein, they are henceforth described as supercavitation.

Fine-scale instabilities associated with laminar–turbulent transition in the separating shear layer at cavity detachment are present for all σ values and are the dominant mechanism for cavity breakup at the higher σ values ($1.0 > \sigma > 0.95$) where cavity lengths are short. At intermediate σ values, where cavity lengths become sufficient for re-entrant jet phenomena to form, the fine-scale instabilities remain active in cavity breakup where fluctuations permit only short cavities to form; bubble clouds are also generated by turbulent engulfment of vapour volumes after cavity collapse.

3.1. *Cavity interfacial phenomena and interaction with upstream boundary layer*

For all cavitation numbers the structure of the cavity leading edge is complicated by viscous and surface tension effects, as shown in figures 3 and 4. As mentioned earlier, the flow detachment phenomenon is described in detail by Franc & Michel (2004) and Brennen (1995); the influence of surface tension is particularly addressed by Tassin Leger & Ceccio (1998) and Tassin Leger *et al.* (1998). For the present case, with a hydrophilic solid surface, the cavity leading edge is convex due to surface tension effects; the laminar nature of the separating shear layer is apparent from

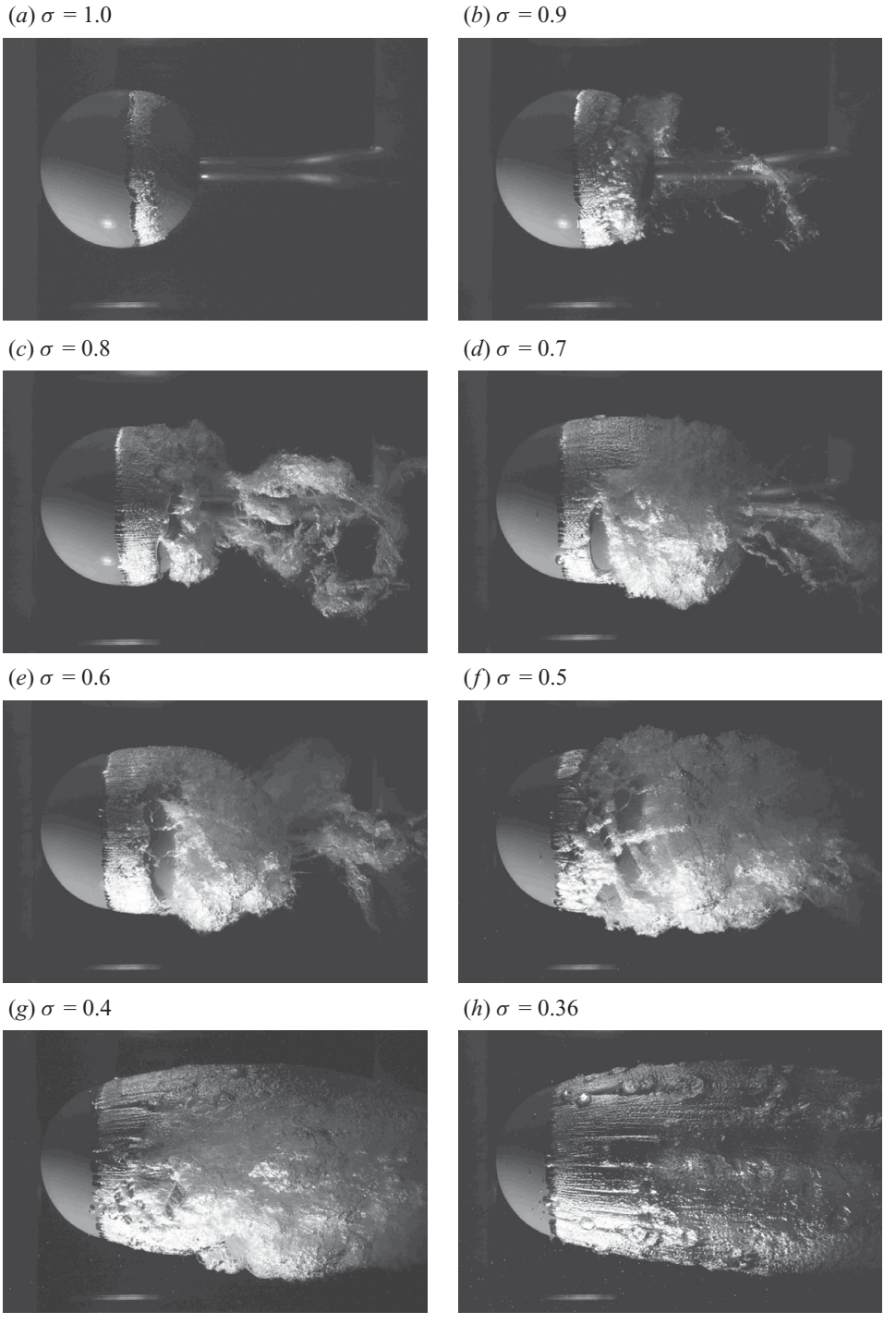

FIGURE 2. Low-speed photography of cavitation occurrence at several cavitation numbers, $Re = 1.5 \times 10^6$.

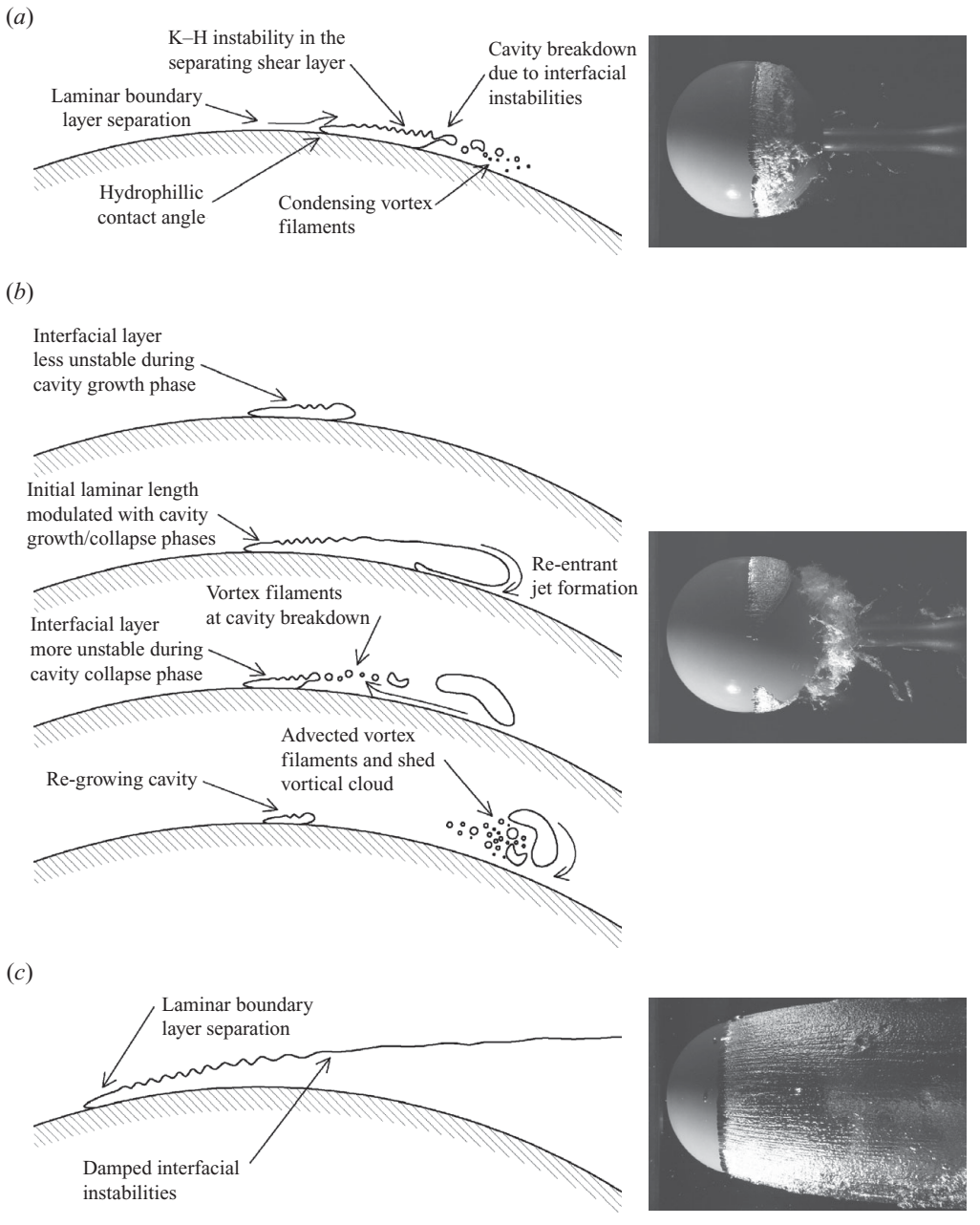

FIGURE 3. Schematic depiction of three modes of cavitation occurrence about the sphere from inception to supercavitation as a function of cavitation number, together with sample photographs. (*a*) $1.0 > \sigma > 0.95$: short cavities with breakup due to fine-scale (K–H) interfacial instabilities. Photograph $\sigma = 0.95$. (*b*) $0.9 > \sigma > 0.4$: cavity lengths become sufficient for re-entrant jet phenomena to occur dominating cavity breakup with large vortex shedding and cloud formation. Sequence depicting a cycle of shedding; photograph $\sigma = 0.9$. (*c*) $\sigma < 0.4$: cavity lengths extend to supercavitation after which re-entrant jet phenomena no longer affect cavity breakup. Photograph $\sigma = 0.36$.

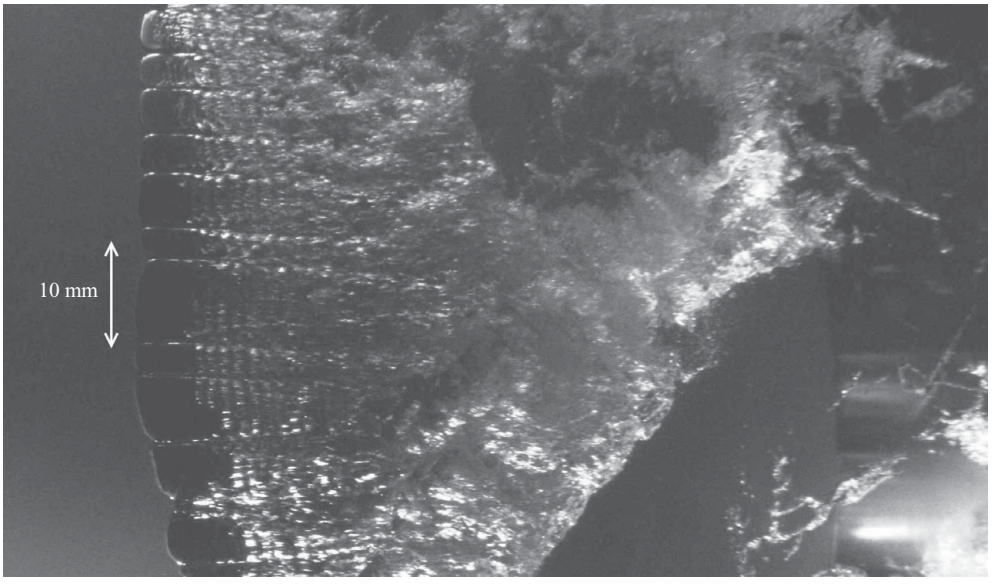

FIGURE 4. Typical cavity leading edge structure of laminar cells and divots at $\sigma = 0.9$. Also showing circumferential K–H instability waves and superimposed streamwise vortex structures in the separating shear layer.

the glassy cavity surface. The location of cavity detachment is determined by the pressure distribution resulting from the combination of wetted flow and separating cavity. As noted by Franc & Michel and Tassin Leger *et al.*, the location of the laminar boundary layer separation, and indeed its existence, differs from the case of fully wetted flow. Furthermore, the location of the boundary layer separation is not identical with the cavity leading edge position. The pressure ahead of the cavity must actually be lower than the cavity pressure, due to the requirement for an adverse pressure gradient for boundary layer separation to occur. Hence entrained cavitation nuclei may be activated near the pressure minimum, forming large bubbles that temporarily break up the sheet cavity leading edge as shown in some photographs of figure 2. The behaviour and influence of such bubbles on the cavity are discussed below.

Figure 4 (for $\sigma = 0.9$) shows the cavity leading edge to be structured in cells of approximately uniform circumferential spacing, on each of which the initial laminar flow is destabilized with the formation of transverse waves from K–H instability in the separated shear layer. The streamwise wavelength, λ, measured from the low-speed photographs gives about 1.35 mm for all cavitation numbers. Taking limiting values for the velocity in the critical layer for $\sigma = 0.9$ as being $U/2 = 6.3\ \mathrm{m\,s^{-1}}$ at separation, and $U = 12.6\ \mathrm{m\,s^{-1}}$ in the limit of the decay of the free shear layer gives the corresponding frequency $f = \overline{U}/\lambda$ in the range 4.7 to 9.3 kHz. This may be compared with the measured frequency of about 8 kHz from high-speed photography taken at a frame rate of 20 kHz.

Ho & Huerre (1984) give $f = 0.032\overline{U}/\theta$ as the frequency for the maximum K–H wave amplification rate in a free shear layer, where $\overline{U}$ is the mean velocity in the shear layer and θ is the momentum thickness. At the point of separation, where $\overline{U} = U/2$, this corresponds to $f = 0.016U/\theta$. Using the surface pressure distribution data of Fage (1936) for subcritical single-phase flow, the laminar boundary layer thickness

θ at separation computed by Thwaites' method with the Mangler transformation is estimated to be about 0.035 mm. Combining with $U \approx 12.6$ m s^{-1} at separation (where the cavity interfacial layer commences) gives $f \approx 6$ kHz. This is in reasonable agreement with the observed and expected frequencies discussed above, and provides strong evidence that the observed waviness of the interfacial layer is due to inviscid instability in the adjacent shear layer: the frequency of progressive capillary waves would be an order of magnitude higher.

Over a similar range of momentum thickness Reynolds numbers for the separated shear layer from an ogival-shaped headform, Brennen (1970*a*) observed a dimensionless instability frequency of $2\pi f\theta/U \approx 0.2$ which corresponds to $f = 0.032U/\theta$. This corresponds to the Ho & Huerre expression with $\overline{U}$ replaced by U, suggesting that the wave activity is occurring far downstream of separation where the velocity differential across the shear layer has largely decayed. This is consistent with the above observation for the cavitating sphere indicating a measured instability wave frequency close to the upper limit estimated from $\overline{U} = U$.

The growth of the transverse waves and their effect on the cavity breakup and shedding behaviour depends on the cavitation number, as this influences both the position of flow detachment and the cavity surface velocity. Figure 4 provides a brief summary and schematic description of the behaviour and effects of the transverse waves. Observations from low- and high-speed photography show the waves to have the greatest influence on cavity breakup at the higher cavitation numbers. The angular position of flow detachment increases almost linearly with cavitation number for $0.36 < \sigma < 1.0$ (figure 10). A corresponding increase in the length of laminar flow near the cavity leading edge is observed as the cavitation number decreases, indicating a lower degree of wave amplification at separation. The later turbulent breakdown at lower σ values will be less vigorous due to the reduced velocity differential across the shear layer at transition onset.

For incipient cavitation at $\sigma \approx 1.0$ (figure 2*a*) turbulent flow appears very rapidly and the cavity is short. The cavity length is stable with uniform breakup of the trailing edge into cavitating vortex filaments, of the scale of the instabilities described, with almost immediate condensation. The cavity length increases steadily as σ is reduced, as shown by the sequence of still photographs in figure 2. At $\sigma = 0.95$ high-speed photography shows the interfacial instabilities to be the main mechanism for cloud formation. The interfacial instabilities remain the main mechanism for cloud formation, but with the increased cavity length the shed volumes remain sufficient for occasional formation of coherent vortical structures downstream of the breakup zone. With further decrease in the cavitation number, cavity lengths become sufficiently large for re-entrant jet phenomena to occur and initiate cavity breakup. The interfacial instabilities still play a local role in regions where circumferential variation in the large-scale shedding permits only short cavities to occur. Their effects can also be seen after cavity breakup from a re-entrant jet, with the small scale vortex filaments, as described above, convected into the shed large-scale vortical structures.

The separated shear layer gradually becomes more stable as σ is reduced. In the supercavitating regime for $\sigma < 0.4$ the cavity leading edge continues to exhibit an initial length of laminar flow with transverse instability waves on the interfacial surface. Further downstream the surface becomes mottled, indicating the presence of turbulent flow in the adjacent shear layer, but is sufficiently glassy for re-entrant jet flow to be seen through the cavity (figure 2*h*). This shows that although transition to turbulence has occurred in the separated shear layer the associated turbulent pressure fluctuations are insufficient to create bubble formation. Fluid at the cavity surface

is rapidly accelerated downstream of the cavity leading edge, due to viscous and turbulent shear stresses in the overlying shear layer. This progressively reduces the shear layer velocity differential and the maximum velocity and pressure fluctuations experienced in a turbulent shear layer. Thus the local Weber number based on turbulent kinetic energy (Hinze 1955) will eventually fall below the critical level required for vapour bubble entrainment at the interfacial surface. Surface tension may also play a role by damping K-H instability in the separated shear layer.

The general dynamic behaviour described above was evident from the high-speed photography for all cavitation numbers. In each case where a local increase in cavity length occurred or a new cavity formed from circumferential variation in the large-scale shedding, the flow detachment location could be seen to move forward on the sphere surface with an associated increase in the initial laminar length of the interfacial layer. This indicates that fluctuations in the bulk flow due to large-scale shedding phenomena momentarily alter the stability of the separating shear layer. The dynamic behaviour of the cavity and interfacial layer is discussed further below.

The interfacial layer exhibits two types of circumferential periodicity (analogous to spanwise periodicity in two-dimensional flows) at all the cavitation numbers investigated, as shown in figure 4. The smaller-scale periodicity is associated with instability phenomena in the separated shear layer. The large-scale periodicity arises from surface tension phenomena at the cavity leading edge.

As discussed by Ho & Huerre (1984), single-phase plane mixing layers exhibit fine-scale spanwise-periodic streamwise streaks caused by secondary counter-rotating streamwise vortices superimposed on the primary rolls generated by the K-H instability; the average spanwise spacing of these streaks is of the same order of magnitude as the local shear layer thickness. For the sphere flow investigated here the fine-scale streaks have a spanwise spacing of about a quarter of the streamwise (K-H) wavelength (or around 0.3 mm), and the estimated shear layer thickness at separation is about 0.25 mm: thus the smaller-scale periodicity appears consistent with the secondary flow mechanism observed in single-phase mixing layers.

3.2. *Divot formation*

The larger-scale streaks dividing the cavity leading edge into cells involve a range of interacting mechanisms in their formation and growth. Tassin Leger & Ceccio (1998) and Tassin Leger *et al.* (1998) present observations of the leading edge features of ventilated cavities for both hydrophobic and hydrophilic surfaced spheres for $1 \times 10^5 < Re < 3 \times 10^5$, and provide a review of earlier work on this topic. A division of the cavity leading edge into cells similar to those observed in the present investigation was observed for the hydrophilic sphere but not the hydrophobic sphere. Tassin Leger *et al.* described this feature in terms of indentations in the cavity leading edge, termed 'divots' throughout the discussion. The divots were observed to exhibit considerable dynamic behaviour including ongoing formation, spanwise movement, coalescence and disappearance.

For the present study, at $\sigma = 0.95$, high-speed photography showed the divots to vary in number or circumferential density with the pulsation in cavity length associated with shedding. With each shedding cycle the cavity length initially increased, followed by breakup due to the interfacial instabilities. During the growth phase, the cells tended to merge and the number of divots decreased. During the collapse phase turbulent mixing would propagate upstream, interacting with the laminar leading edge and triggering the formation of new divots with a much finer cellular division

that subsequently merged again with cavity regrowth. With the formation of new divots, wedges of mixing could be seen developing from them indicating the presence of associated streamwise vortices. A similar modulation of the divot density with cavity shedding was observed for $\sigma = 0.9$.

At $\sigma = 0.8$ shedding and cloud formation become more coherent, with frequent events of large-scale shedding and leading edge extinction as shown in the photo sequences in figures 5 and 6. Following a large-scale extinction, re-nucleation is seen to be of two forms. Nucleation begins with activated nuclei stretched to have a streak-like (glassy) appearance; as they are convected downstream they become fleck-like (mottled), as shown in the magnified photo sequence in figure 7. The streak-shaped bubbles are some 5 to 10 mm upstream of the fleck-shaped bubbles, as shown in the second row sequence in figure 7. This streak- and fleck-like nucleation is thought to be associated with laminar–turbulent boundary layer transition in fully attached flow. New streaks form continuously around $\phi = 88^\circ$ in the laminar flow region immediately downstream of the pressure minimum for steady single-phase flow. The subsequent appearance of the flecks around $\phi = 97^\circ$ agrees well with the Achenbach (1972) observed location of transition at this Reynolds number. The flecks apparently result from the diffusion of streaks by turbulent mixing. The streak-shaped bubbles, being nuclei-activated close to the pressure minimum, were seen to form continuously in regular circumferentially preferred locations, as shown in the third and fourth row sequences in figure 7. The circumferential spacing (averaging around 5 mm) is commensurate with estimated Tollmien–Schlichting wavelength just downstream of the pressure minimum, suggesting three-dimensional instability of the attached boundary layer may have a significant influence on the developing structure of the cavity leading edge.

Repeated nucleation by this process eventually generates sufficient vapour/gas volume to establish a macroscopic cavity. The nucleating streaks are thus precursors in the initial formation of the leading edge cells, with divots being the remnant gaps between the streaks. Further streamwise vorticity is generated by local secondary flow arising from circumferential variations in the cavity leading edge thickness associated with the divots. With formation of the sheet cavity, the cells were seen to merge as the cavity grew in length, similar to the behaviour with the higher cavitation numbers described above. Similar general behaviour was observed for $\sigma < 0.8$ where leading edge extinction occurred, although the sequence involved less transients with the leading edge reforming at a faster rate as the cavitation number was reduced. With the onset of supercavitation the cells became relatively stable, undergoing only local reorganization with disturbances caused by passing bubbles or the occasional influence of a re-entrant jet.

The relationship between divot formation and the cavity leading edge nucleation/formation process and the presence of associated vortices show the divots to be the result of dynamic interaction with the transitioning laminar boundary layer. Three regimes are evident depending on the shedding behaviour. At the high cavitation numbers, where the cavity leading edge is ever present, the divot spacing is modulated periodically with cavity collapse and regrowth. In the collapse phase divot numbers increase from the disturbance of the forward encroaching turbulent shear layer; in the growth phase their numbers decrease with the more stable conditions of the locally accelerating outer fluid. For the case where shedding causes leading edge extinction, spanwise perturbations in the separating boundary layer create preferred circumferential sites for nucleation involving streak-like bubbles; these enhance secondary flows that eventually merge to form the cellular leading edge.

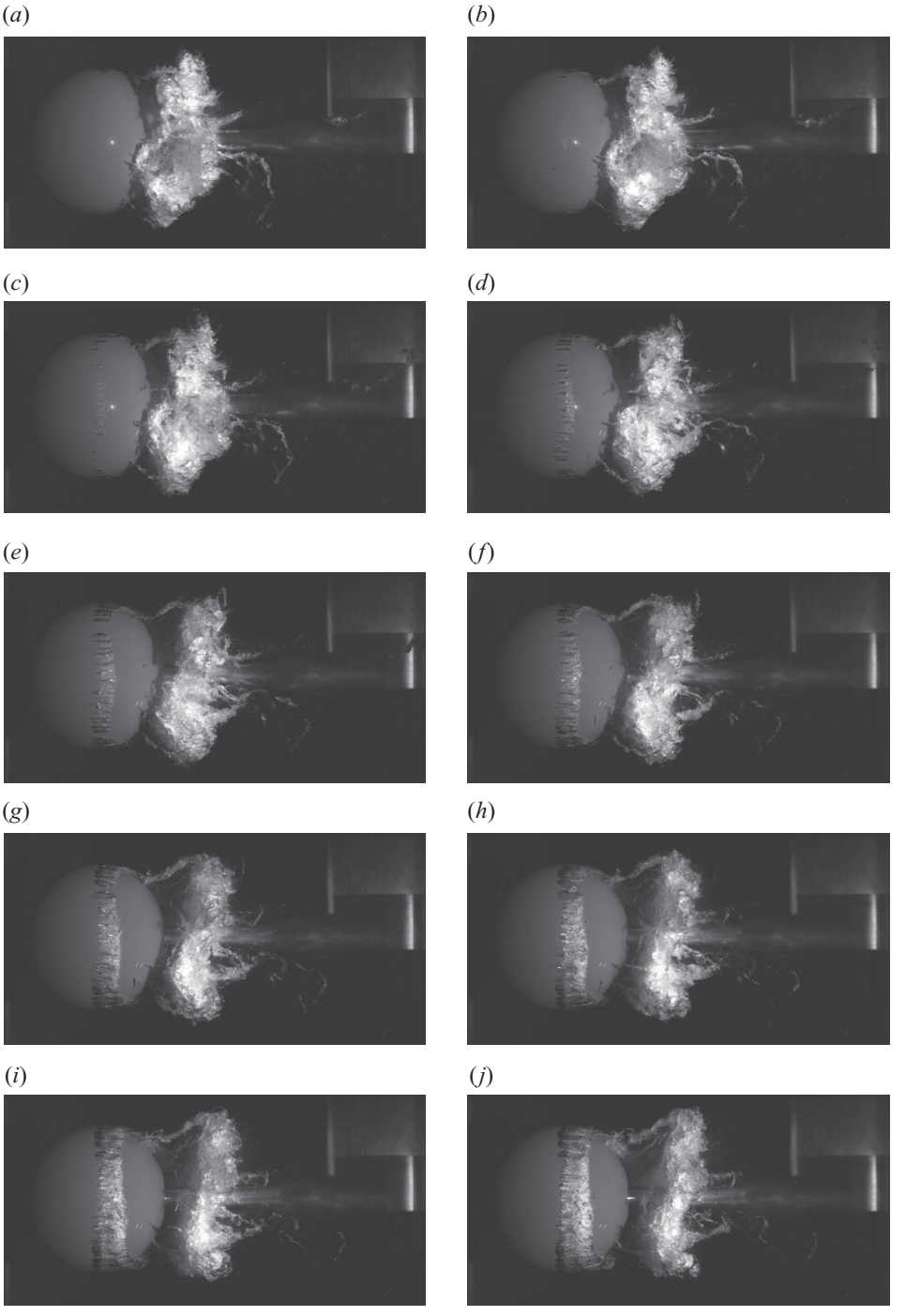

FIGURE 5. Sequence of extracted images from high-speed photography at $\sigma = 0.8$, separated by 1.17 ms (frames 3636–3699, in seven frame increments), showing inception and regrowth of the sheet cavity after the previous cavity was completely shed.

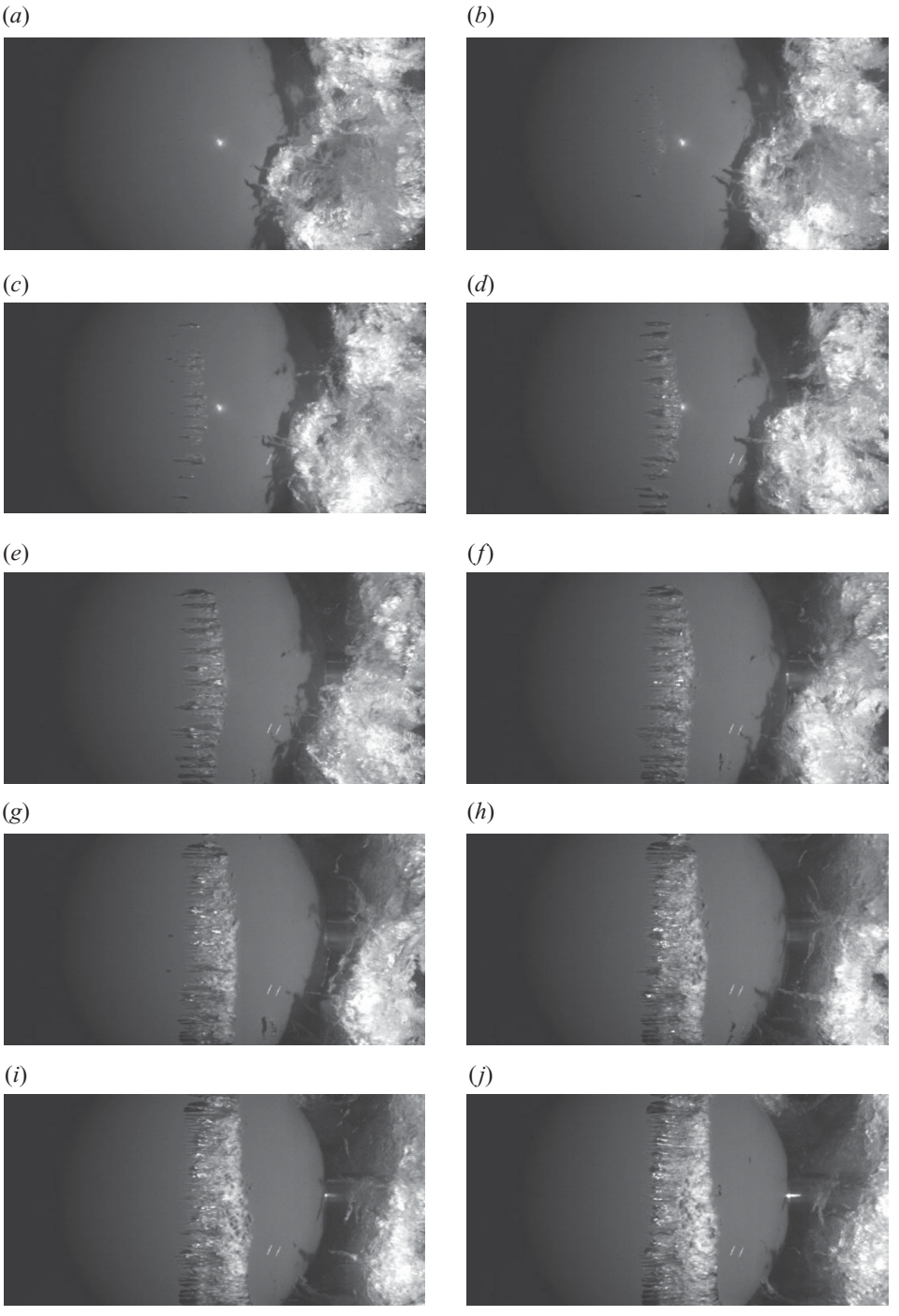

FIGURE 6. Sequence of magnified images from figure 5. Nucleation appears initially as teardrop-shaped (glassy) streaks that are convected downstream becoming flecks (mottled) associated with laminar–turbulent boundary layer transition. The streaks form continuously at regular circumferentially preferred locations growing and merging to form the cellular cavity leading edge structure.

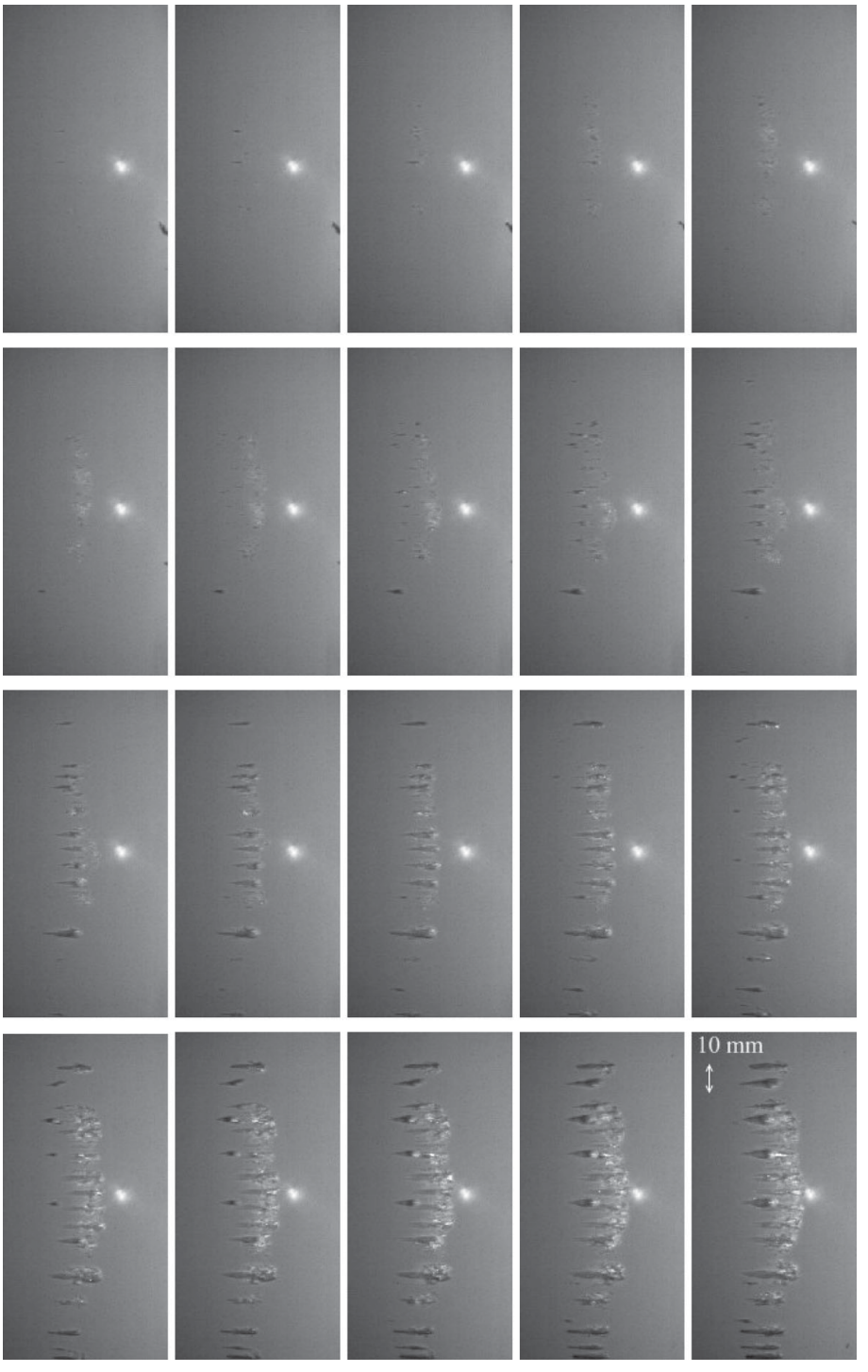

FIGURE 7. Sequence of magnified images from figures 5 and 6 separated by 0.17 ms (frames 3636–3655, in single-frame increments). Nucleation appears initially as teardrop-shaped (glassy) streaks that are convected downstream becoming flecks (mottled) associated with laminar–turbulent boundary layer transition. The streaks form continuously at regular circumferentially preferred locations growing and merging to form the cellular cavity leading edge structure.

In the stable conditions created by supercavitation the divot/cell structure becomes relatively stable.

3.3. *Interactions with bubbles travelling in the free stream*

For $\sigma \leqslant 0.7$, including cases with supercavitation, bubbles were regularly seen to form and grow rapidly upstream of the cavity leading edge; they generally caused local cavity breakup, as shown in the photo sequence of figure 2. Li & Ceccio (1996) describe extensive observations of the interaction of travelling bubbles with the boundary layer and attached cavitation on a hydrofoil. Similar interactions to those described by Li & Ceccio were observed in the present study.

The extent of these interactions depended on the size to which bubbles grew and the timing of the encounter within the shedding cycle. The bubbles were roughly circular in planform, with diameters varying from about 1 to 15 mm when reaching the leading edge. A sequence typical of the growth and interaction with the cavity of a larger-size bubble is shown in figure 8. The large bubble in the sequence is initially discernible about one-quarter sphere diameter upstream of the cavity leading edge. The oblate-shaped bubble exhibits a diameter growth rate of about 6 $\mathrm{m\,s^{-1}}$, and reaches a diameter of about 15 mm when centred on the cavity leading edge. The bubble convection speed is about 12 $\mathrm{m\,s^{-1}}$. As the bubble reaches the leading edge, small cavitating tails at each side can be seen (figure 8*d*) resulting from boundary layer interaction and the formation of secondary flows. Li & Ceccio (1996) describe interactions of single bubbles with a boundary layer in a non-cavitating flow and discuss the development of related secondary flows. They also show that bubbles may induce local transition in unstable boundary layers, resulting in the formation of turbulent cavitating tails. No such phenomena were observed in the present study, although evidence of turbulence in the bubble wake may be seen in the sweeping away of the cavity leading edge as described by Briançon-Marjollet, Franc & Michel (1990) and Li & Ceccio. The characteristic 'fork'-shaped cavity portion in the bubble wake, described by Li & Ceccio, is clearly evident in figure 8(*d*). The cavitating secondary flows at each spanwise edge were only seen for the largest of bubbles, indicating for the present boundary layer conditions a critical bubble size for their formation. At the lower cavitation numbers, with the associated forward movement of the cavity, bubbles had less time to grow before encountering the cavity leading edge; this resulted in smaller bubbles and no cavitating secondary flows.

Bubbles had the greatest effect on formed or growing sheet cavities where, as shown in figure 8, the cavity and its leading edge were broken due to the obstruction caused by the bubble and its trailing turbulent wake. With encounters where the cavity was in the last stage of collapse, or was re-nucleating after leading edge extinction, bubble obstruction caused breakup of the leading edge only; the bubble was consumed thereafter by the encroaching turbulence. No evidence was observed for bubble entrainment playing any role in initiating collapse of a sheet cavity.

The passage of all but the smallest bubbles would form a new divot in the cavity leading edge. For formed or growing cavities the divot/cell structure is locally reorganized with the passing of a bubble. For larger bubbles, particularly where several cells were swept away, the leading edge was seen to close after bubble passage by widening of the adjacent divot cells. With full closure of the leading edge and divot formation, the adjacent widened cells would then divide and form new divots. This process is similar to the modulation of the cell/divot circumferential density with cavity growth/collapse described earlier, due to local acceleration creating a temporary stabilizing effect.

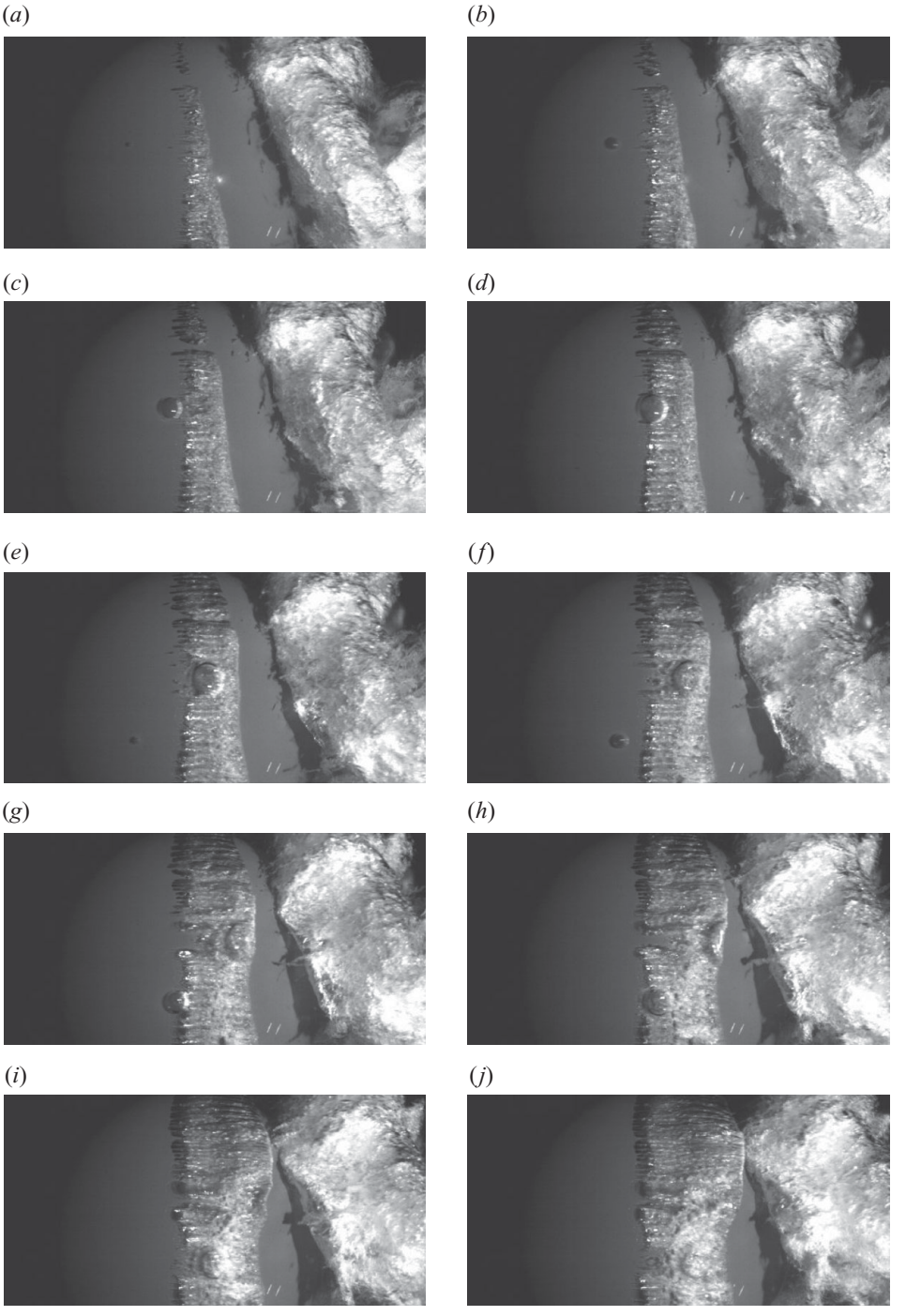

FIGURE 8. Sequence of extracted images from high-speed photography, separated by 0.83 ms (frames 3419–3464, in five frame increments), showing activated nuclei upstream of the cavity leading edge causing momentary local cavity breakup, $\sigma = 0.7$.

3.4. *Cavity leading edge dynamics*

The circumferential mean location of the cavity leading edge observed in the present study at $Re = 1.5 \times 10^6$ varied linearly from 97° to 72° from the sphere front stagnation point with reduction in σ from 1.0 to 0.36, as shown in figure 10. These results are consistent with various data presented by Brennen (1995) for a range of Reynolds numbers, cavitation numbers and tunnel blockage ratios. However, they differ significantly from data for single-phase flow. Achenbach (1972) reports separation from a smooth sphere with about the same free stream turbulence intensity (around 0.5 %) varying from 83° for subcritical flow ($Re = 2 \times 10^5$) to 120° for supercritical ($Re = 4 \times 10^5$), and remaining approximately constant above and below these Re values.

Times series data derived from high-speed photography showed the cavity leading edge location to behave dynamically depending on shedding behaviour and hence cavitation number. As mentioned earlier, at intermediate cavitation numbers where large-scale shedding phenomena occurred this was frequently accompanied by large-scale leading edge extinction. Figure 9 shows examples of time series data derived from high-speed photography for cavitation numbers of 0.8 and 0.9. Small-scale shedding occurs for the $\sigma = 0.9$ case, while large-scale shedding occurs for the $\sigma = 0.8$ case. The quantity plotted for analysing shedding dynamics (bottom plots of figures 9*a* and 9*b*) is the spatial average light intensity of the 10 × 25 pixel region B within the shedding region defined in figure 1.

For detection of the streamwise mean cavity leading edge location, data for a 25 pixel spanwise region A, also shown in figure 1, were analysed (middle plots of figures 9*a* and 9*b*), from which leading edge extinction events were flagged (top plots of figures 9*a* and 9*b*). Both regions A and B, although not aligned in the streamwise direction, were chosen on the basis of favourable light intensity and contrast. The region A chosen for leading edge detection showed the best contrast between cavity leading edge and background sphere surface light intensity. The criterion for defining leading edge presence was an edge detection for at least one of the 25 sampled spanwise pixels within ±50 streamwise pixels of the mean detachment location.

The cavity leading edge time series for $\sigma = 0.9$ (figure 9*a*) shows the leading edge to be present almost continuously with only two brief extinction events. At $\sigma = 0.9$, cavity lengths become just large enough for the re-entrant jet to become the dominant mechanism in cavity breakup. Shedding is coherent and predominantly axisymmetric, but with occasional events of non-axisymmetry with simultaneous circumferential regions of cavity growth, collapse and shedding. The first extinction event shown in figure 9(*a*) corresponds to an axisymmetric shedding event where almost all of the visible leading edge, except for some nucleating flecks, was extinguished. This time series shows the reforming leading edge moving to a downstream limit and then with sheet cavity growth retreating upstream. The second extinction corresponds to a non-axisymmetric event where the leading edge is shed only locally, and without large-scale movement of the bulk flow. There is then no corresponding downstream maximum in the leading edge location, and the leading edge location is modulated by cavity shedding with a fluctuation amplitude related to the magnitude and extent of each event. The location of the two sampled regions, although not aligned in the streamwise direction, is sufficiently close that the number of events in each coincide: the number of maxima in the leading edge location and the number of distinct events in the pixel intensity are each nominally 33. The greatest maxima in leading edge excursions correspond to shedding events where, although the cavity is shed, the leading edge remains nucleated in flecks presumed associated with boundary

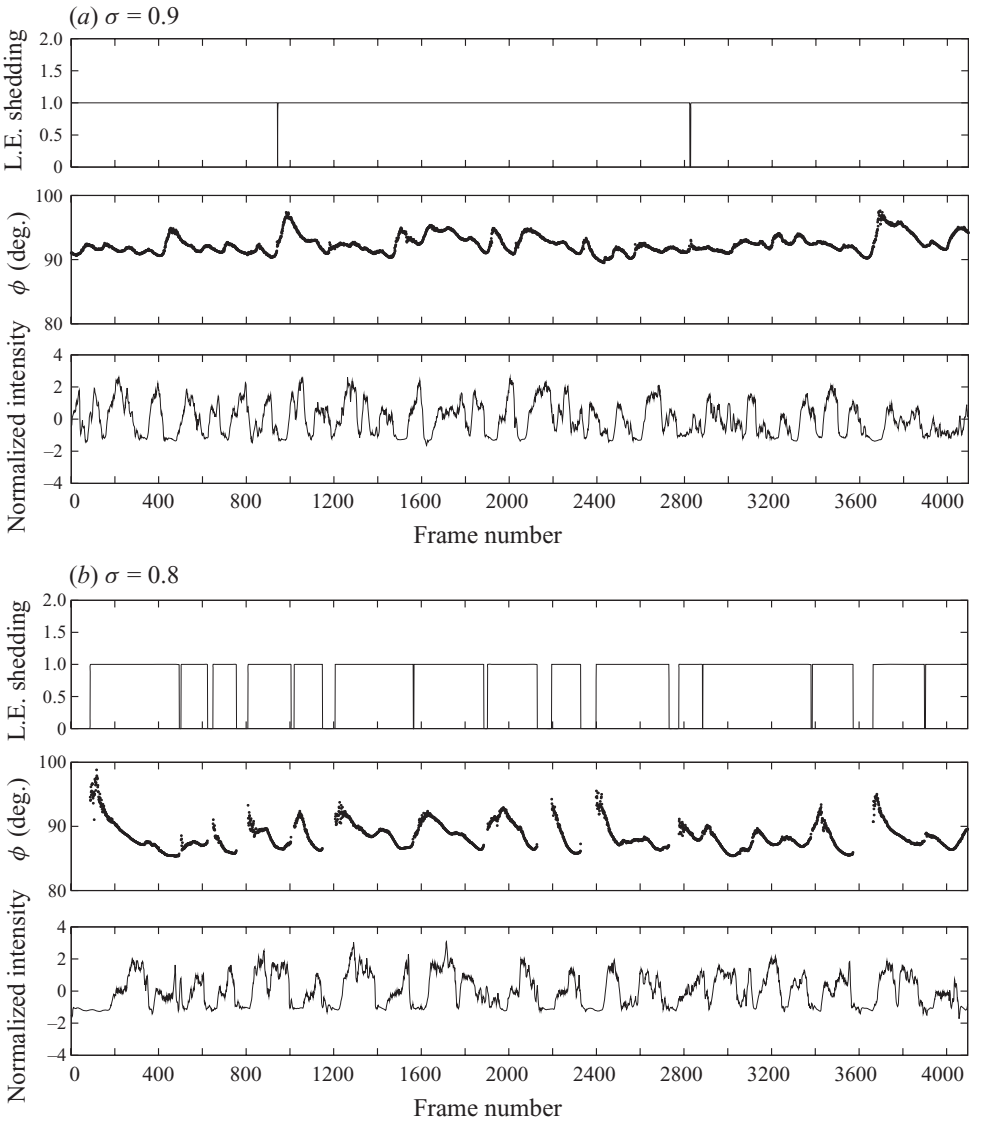

FIGURE 9. Time series data derived from high-speed photography from sampled regions A and B (see figure 1) showing correlation of cavity leading edge and shedding dynamics for (*a*) $\sigma = 0.9$; (*b*) $\sigma = 0.8$. (Top) flagged leading edge shedding events from sampled region A, (middle) cavity leading edge angular position ϕ measured from front stagnation from sampled region A and (bottom) spatial average pixel intensity of sampled region B in the shedding zone.

layer laminar–turbulent transition, as described above. The minima in leading edge excursions correspond to the growing cavity achieving maximum length prior to breakup. From this time series the maximum leading edge location was about 98° from the front stagnation point, with a minimum of 90° and a mean of 92°.

For $\sigma = 0.8$ cavity lengths become sufficient for large-scale shedding to occur, with more frequent leading edge extinctions observed every one to three shedding events. Sample sequences of large-scale leading edge extinction events for a cavitation number of 0.8 are shown in figures 5, 14 and 15, with the frame numbers noted

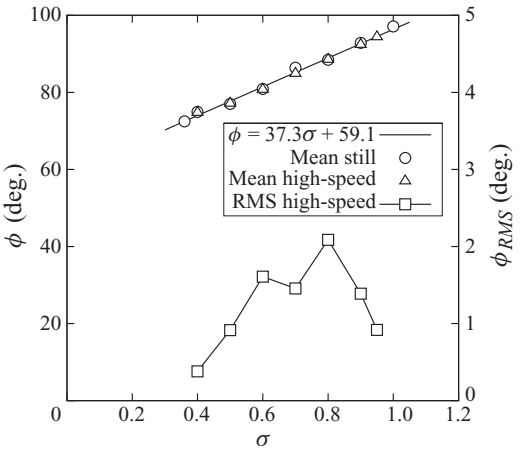

FIGURE 10. Mean angular location ϕ and RMS fluctuation of cavity leading edge position ϕ_{RMS} measured from front stagnation point derived from low- and high-speed photography.

corresponding to the time series shown in figure 9(*b*). As for $\sigma = 0.9$, the amplitude of leading edge movement depends on the magnitude and extent of the shedding event. The first extinction event shown in figure 9(*b*) corresponds to a large-scale or long duration event where all the visible leading edge was extinguished (figure 14*a*). This extinction corresponds to the shedding of a near complete vortical ring, except for a section that remains attached on the far side of the sphere. This particular event is discussed in detail below in § 3.5; it is typical of the longer duration extinctions shown in figure 9(*b*) where circumferentially large portions of the cavity are coherently shed. Events where the leading edge undergoes small amplitude excursions, with short durations of extinction, correspond to local circumferential shedding. For these events the shedding is more oblique, with circumferential regions of cavity growth connected to already shed cavities typical of the sequence shown in figure 14(*g–l*). This time series indicates a maximum leading edge location of about 99°, a minimum of 81° and a mean of 89°.

With reduction of σ below 0.8 the shedding frequencies are reduced by the increasing cavity length; hence the frequency of leading edge extinction events is also lowered. The duration of extinction is correspondingly reduced, with re-nucleation occurring more rapidly with reduction in the cavitation number. For $\sigma < 0.4$ supercavitation ensues and the leading edge is present continuously; its location is then stable with only small fluctuations.

To make an overall comparison of leading edge extinction phenomena for all cavitation numbers tested, some basic statistics are presented in figures 10 and 11. Figure 10 shows the RMS fluctuations of the cavity leading edge location as a function of cavitation number. Figure 11 shows the leading edge presence (t_{LE}, defined as the fraction of time present for the 25 pixel spanwise sampled region A shown in figure 1) and the number of leading edge shedding events as a function of the cavitation number. Figure 10 shows the RMS leading edge fluctuation for a cavitation number of 0.95 (where cavity breakup is dominated by interfacial instability) to be about 1° or 13 mm of surface arc length. The RMS value increases linearly to a maximum of about 2° at a cavitation number of 0.8, where shedding is coherent and breakup is due to re-entrant jet phenomena. With further decrease in cavitation number the RMS value decreases approximately linearly to about 0.4° at a cavitation number of

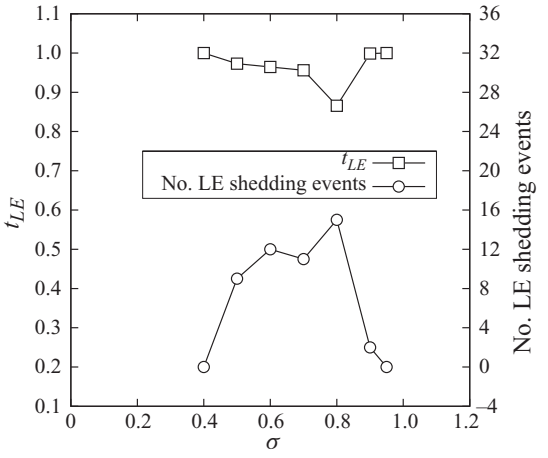

FIGURE 11. Leading edge presence (t_{LE}) and number of leading edge shedding events as a function of cavitation number derived from high-speed photography record of duration 683 ms (t_{LE}, defined as the fraction of time present for the 25 pixel spanwise sampled region A shown in figure 1).

0.4 for which marginal supercavitation occurs. Figure 11 shows the leading edge to be present continuously for $\sigma = 0.95$ and 0.4, the largest and smallest cavitation numbers tested, and t_{LE} to reach a minimum of 0.87 at $\sigma = 0.8$ where the shedding is most coherent. For lower cavitation numbers the leading edge, although shed, is rapidly re-nucleated; t_{LE} remains roughly constant at about 0.96. The number or frequency of events shows the sudden increase in leading edge shedding that occurs once the re-entrant jet becomes the mechanism for cavity breakup. Although the number of events is a maximum at $\sigma = 0.8$, it only varies between 9 and 15 for $0.5 < \sigma < 0.8$.

3.5. *Shedding and coherence of the cavitating wake*

To investigate the coherence and frequency content of cavity shedding a wavelet transformation of the light intensity time series from a fixed region within the shedding zone was carried out for all cavitation numbers tested. A single time series for each cavitation number was derived from the spatially averaged pixel intensity of the 10×25 region B indicated in figures 1 and 14. Examples of these data are shown in figure 12 for cavitation numbers of 0.5 and 0.8. The upper plot in each case is the spatially averaged pixel intensity normalized by its standard deviation; the lower plot is the corresponding wavelet transformation and the right-hand plot is the power spectral density normalized by peak intensity. The wavelet transformation is plotted in terms of Strouhal number, $St = fD/U$, where f is the wavelet characteristic frequency. It should be noted that the upper cutoff frequency/Strouhal number is below that required to detect the K-H waves discussed earlier. A contour plot of the normalized wavelet power spectrum against cavitation number is shown in figure 13. At the higher cavitation numbers, just below inception, there is a single or narrow peak in the power spectrum. For cavitation numbers between 0.8 and 0.6 either two frequencies or a broad peak are apparent. At the lower cavitation numbers, approaching supercavitation, shedding behaviour returns to a single or narrow range of frequency. The variation of shedding behaviour with cavitation number, and hence the general spectral characteristics shown in figure 13, are discussed in detail below, i.e. examples of wavelet transformations for typical individual shedding events are

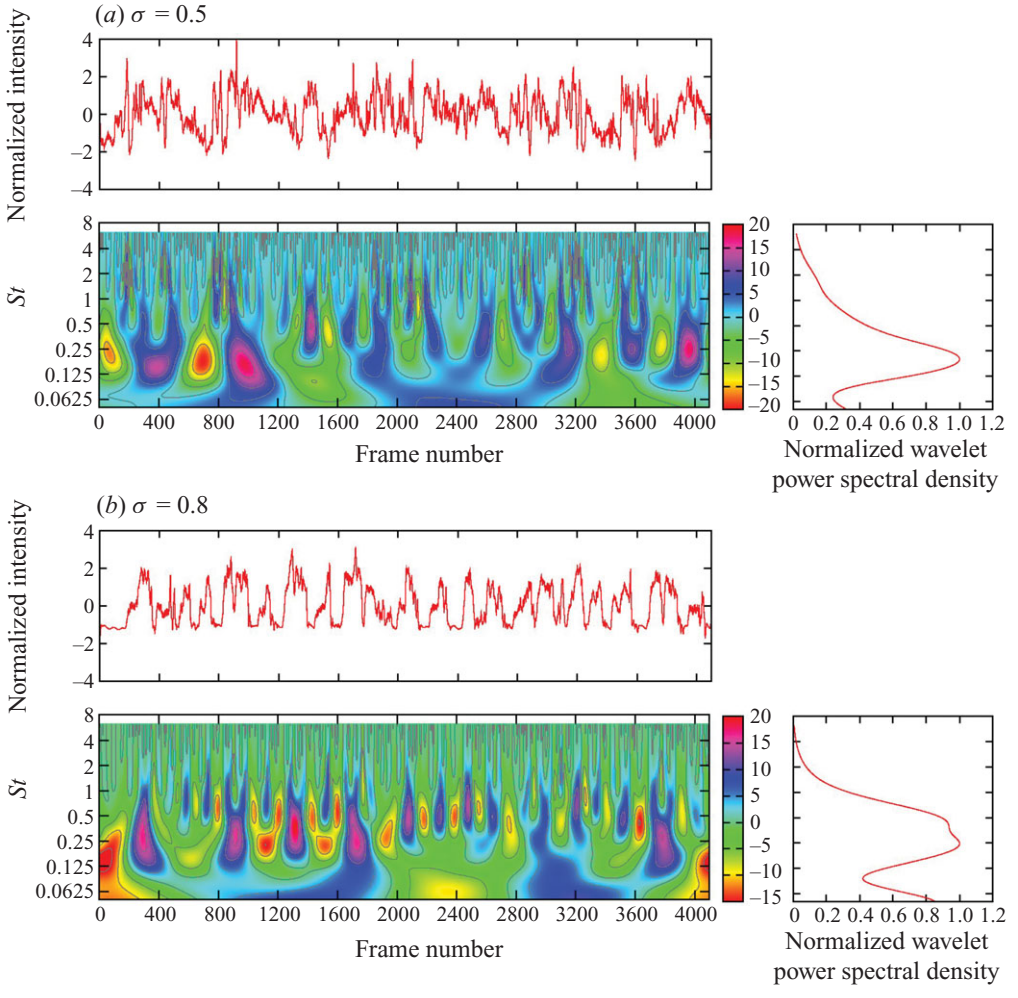

FIGURE 12. Time series of spatially averaged pixel intensity (normalized by standard deviation) for region B within the shedding zone (see figure 1) and corresponding wavelet transformation for (*a*) $\sigma = 0.5$; (*b*) $\sigma = 0.8$. Power spectral density obtained from the wavelet transformation (normalized by peak amplitude).

given. The general shedding behaviour may be described in terms of the relative effects of various phenomena observed in the high-speed photography, some of which have been discussed above (see also figure 3).

For $\sigma = 0.95$, the sheet cavity breaks down to cavitating vortex filaments of the scale of the interfacial instabilities described above. The filaments accumulate just downstream of the breakup area and are shed with a dominant frequency similar to non-cavitating sub-critical flow with $St \approx 0.28$, as shown in figure 13. The sheet cavity length fluctuates with trailing edge breakup and the shedding cloud but its leading edge remains in place virtually all the time.

At $\sigma = 0.9$, cavity lengths become sufficient for a re-entrant jet to form; this directly affects the breakup of the sheet cavity. Initial breakdown typically occurs at about mid cavity length, at several circumferential sites from which fronts emanate; the sheet cavity then breaks down into cavitating filaments as described above. The filaments

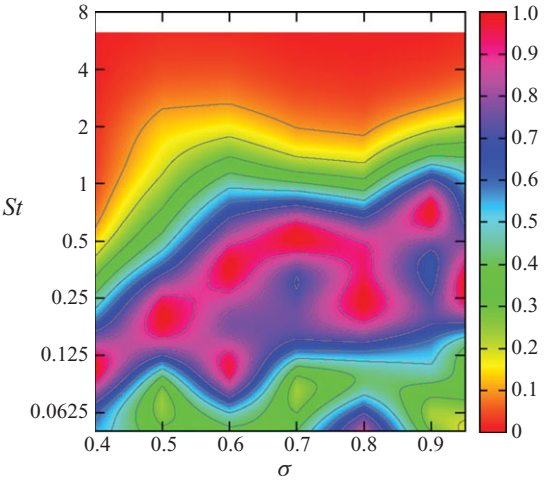

FIGURE 13. Normalized wavelet power spectra of shedding frequencies expressed as a Strouhal number over the range of cavitation numbers for which shedding occurs. (Contour plot derived from power spectra at discrete cavitation number increments of 0.1 between 0.4 to 0.9, and 0.95).

either condense or are shed by advection with the vortical cloud. The formation and shedding of each cloud is close to axisymmetric. Some cycles cause the sheet cavity to be displaced for large lengths of the circumference, but for only a short duration with the cavity quickly growing anew. The power spectrum has two peaks at St values of about 0.2 and 0.72. The duration of each event appears to depend on the cavity length and therefore the time required for sheet cavity growth and re-entrant jet return to affect cavity breakup.

The cavitation behaviour at $\sigma = 0.8$ is similar to that at 0.9, except that maximum cavity lengths become greater and both cavity formation and shedding show larger departures from axisymmetry. Shed cloud cavities and forming sheet cavities interact in a complex way, examples of which are given in figure 14. Figures 14(a–f) and 14(g–l) show image sequences of typical long- and short-duration shedding events respectively. Figure 14(m) shows a segment of light intensity time series data from the sampled region B during these events and the corresponding wavelet transformation.

The sequence of figure 14(a–f) shows the oblique shedding of a near complete vortical ring, except for a section that remains connected to the forming cavity on the far side of the sphere such that a hairpin-like structure is shed. The high-speed photography suggests that, following this event, a symmetric but less intense event occurs on the opposite side of the sphere.

The later event (sequence of figure 14g–l), where cavity lengths are shorter, shows an apparent helical coupling between the shed and forming cavities. The time series data and corresponding wavelet transformation, segments of which are presented in figure 14(m), show these modes to be typical and to characterize the two dominant frequencies in the power spectrum with St values of about 0.24 and 0.4. As shown in the image sequences of figure 14 for $\sigma = 0.8$, the shedding events are of sufficient intensity for large regions of the sheet cavity to be entirely displaced for significant periods of the shedding cycle.

To investigate circumferential correlation of the shedding, time series data from two spanwise regions (similar in dimensions to region B) either side of the vertical

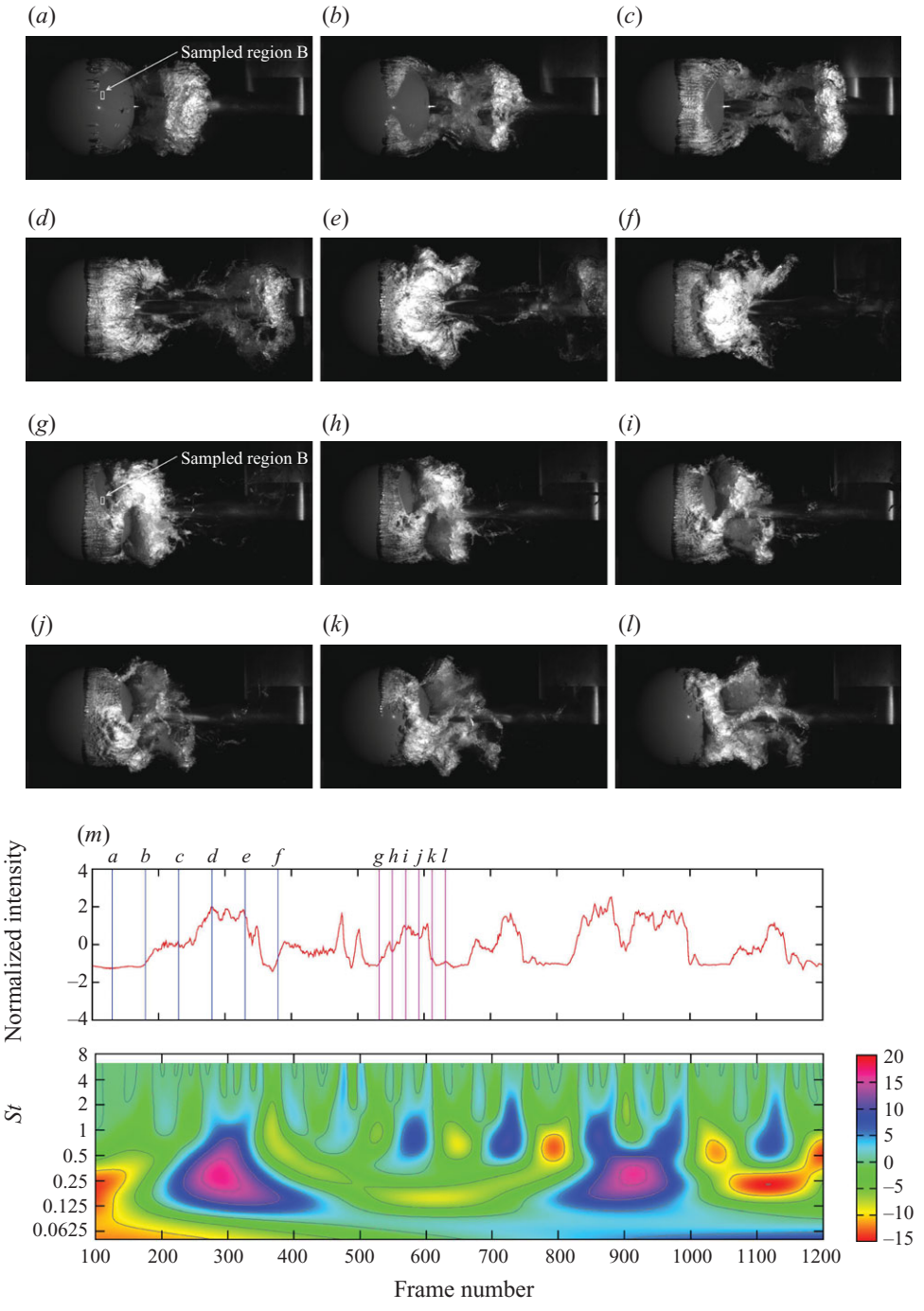

FIGURE 14. Sequence of extracted images from high-speed photography at $\sigma = 0.8$ depicting typical long- (*a–f*) and short-duration shedding events (*g–l*) and (*m*) corresponding segment of light intensity time series data from the sampled region B, with frame sequences marked and the corresponding wavelet transformation. Long duration shedding event depicted in (*a–f*) separated by 8.3 ms (frames 130–380, in 50 frame increments): oblique shedding of a near complete vortical ring, except for a section that remains connected to the forming cavity on the far side of the sphere such that a hairpin-like structure is shed. Short duration shedding event depicted in (*g–l*): apparent helical coupling between shed and forming cavities.

centreline were cross-correlated with time series on the centreline. Cross-correlation of time series for individual shedding events and examining the offsets in the first correlation peak made evident the oblique nature of individual shedding events. Analysis of several shedding events showed the obliqueness of the cavity leading edge and deviation from axial symmetry to vary randomly. Cross-correlation of time series over a large number of shedding events gave no offsets, showing that in the time-mean the shedding is purely axisymmetric.

Cavitation behaviour at σ values of 0.6 and 0.7 shows similar coupling or modulation of forming cavities by those shed as for $\sigma = 0.8$, but with greater maximum cavity lengths and shed cavity volumes. For $\sigma = 0.7$ the peak frequencies of the power spectrum correspond to St values of about 0.2 and 0.52; for $\sigma = 0.6$, the St values are about 0.11 and 0.35. Both these cavitation numbers are sufficiently low that, despite the intensity of the shedding events, the sheet cavity is displaced for only short periods of the shedding cycle.

At $\sigma = 0.5$, cavity lengths have grown to about two sphere diameters. The re-entrant jet behaviour is becoming dominant and tending to be more axisymmetric, causing nearly simultaneous breakdown of the entire sheet cavity circumference. Due to the almost simultaneous breakdown of the entire sheet cavity there is little interaction between shed bubble clouds and newly growing sheet cavities, so that only one dominant frequency is present in the power spectrum shown in figure 13. The presence of cavitating vortices within the interfacial layer can be seen at breakdown of the sheet cavity as is the case for larger cavitation numbers, but with much greater volume as apparent in figure 2. At breakdown a new sheet cavity is initiated almost immediately, following closely ahead of the previously shed cloud.

For $\sigma = 0.4$ the cavity length becomes so large that the re-entrant jet barely reaches the sphere. The returning liquid/vapour mixture is mostly carried back downstream as it impinges on the cavity wall. Due to the greater cavity volume and greater distance travelled by the re-entrant jet there is sufficient time for the jet fluid to fall due to gravity. With the plunging of the re-entrant jet fluid only the bottom of the sheet cavity is affected. With most of the fluid being carried downstream as it impinges on the lower half of the sheet cavity, the well-known 'breaking wave'-type cavity closure occurs. Occasionally sufficient re-entrant jet fluid accumulates to cause a short breakdown of the sheet cavity with the frequency corresponding to $St \approx 0.1$ as seen in figure 13.

Detailed information on the cavity trailing edge during shedding events unfortunately could not be gathered by automated numerical means due to its ill-defined nature. Data were however gathered manually at a fixed vertical ordinate for selected shedding events at cavitation numbers ranging between 0.9 and 0.5. These results show that the cavity growth rate is close to linear for most of the shedding cycle, only becoming mildly nonlinear in the later part approaching cavity breakdown. The growth rate is virtually independent of the cavitation number for about the first half of the shedding cycle at about $0.43U$. In the later part of the cycle the growth rate slightly increases with reducing cavitation number.

For cavitation numbers between 0.8 and 0.5, where re-entrant jet phenomena dominate and shedding is most coherent, the mechanism for sheet cavity breakdown to cloud cavitation can be easily seen. A sample image sequence of sheet cavity breakdown is shown in figure 15 for $\sigma = 0.8$. Initiation of breakdown occurs near the bottom of the sphere, where there is a convergence and accumulation of re-entrant jet fluid that impinges upon the surface of the growing sheet. The impinging fluid creates a perforation in the growing sheet from which a collapse front radiates. The collapse

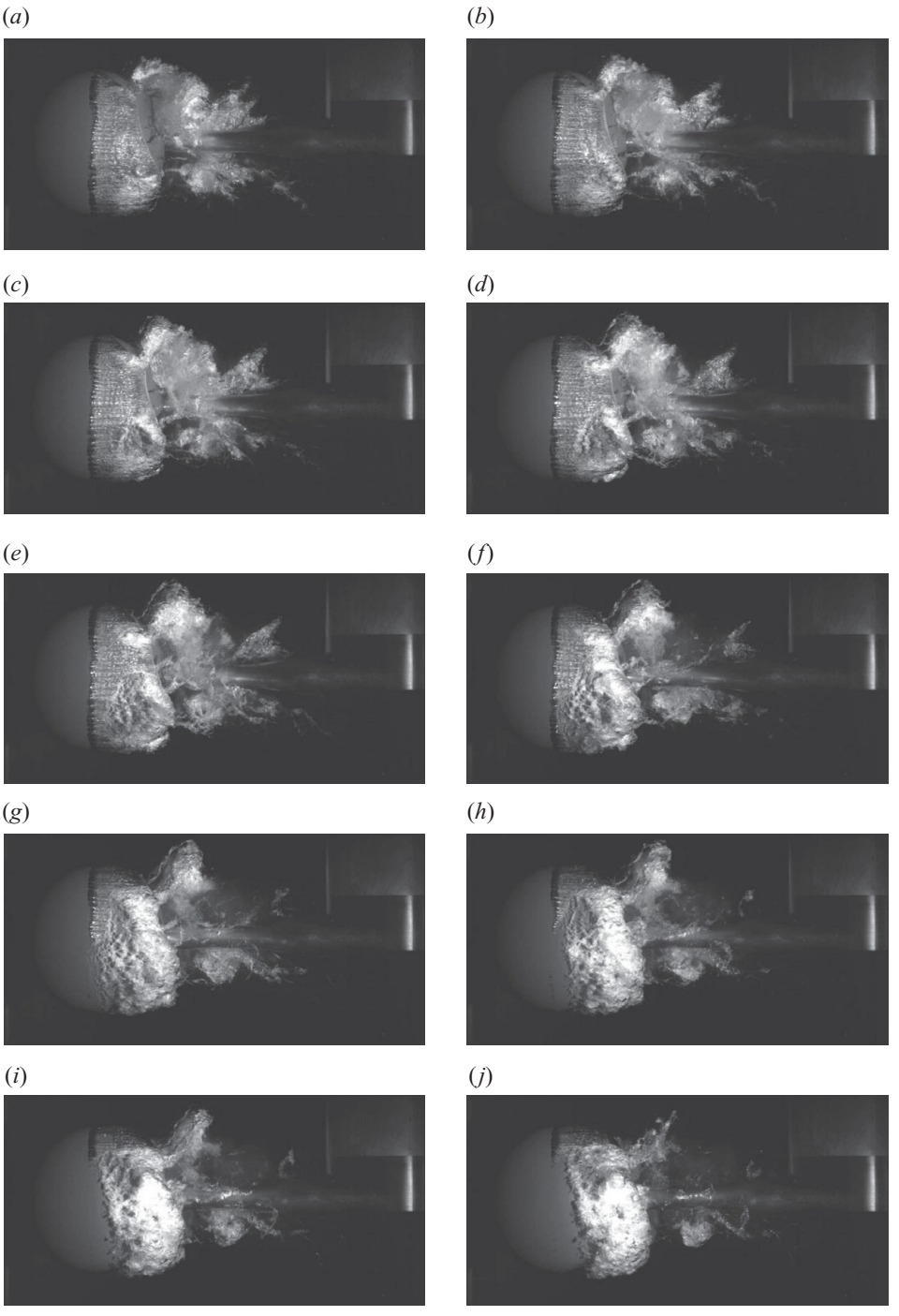

FIGURE 15. Sequence of extracted images from high-speed photography, separated by 1.17 ms (frames 3975–4038, in seven frame increments), showing initial cavity breakup and propagation of the collapse front with remnant condensing vapour convected in shear layer vortices with their eventual coalescence into large-scale cavitating wake vortices, $\sigma = 0.8$ (collapse front propagation speed about $1.3U$).

front travels with approximately equal speed in all directions, reaching the cavity leading edge first and causing large-scale extinction; it then extends across the sphere in the spanwise direction. The propagation speed is about $1.3U$. In the wake of the collapse front, remnants of condensing vapour instantaneously form filaments; these are convected away in shear layer vortices that subsequently coalesce into large-scale cavitating vortical structures in the sphere wake. The speed of the collapse front is consistent with the propagation velocity of a pressure wave in a multiphase flow; the spontaneous reduction of vapour/gas volume in its wake shows the front to be the leading edge of a positive pressure wave emanating from the initial accumulation of bubbly re-entrant jet fluid.

In summary, for high cavitation numbers just below inception, breakdown of the cavity is due mainly to instabilities within the interfacial layer resulting in predominantly axisymmetric shedding behaviour. For intermediate cavitation numbers, where cavity lengths extend up to two sphere diameters, there is a coupling or interaction between shed clouds and growing sheet cavities where two dominant frequencies or a broad peak are present in the wavelet power spectra. As the cavitation number is decreased, cavity lengths become greater making the period for sheet cavity growth and the effect of the re-entrant jet greater and thus reducing the dominant frequencies. There appears to be a limiting cavitation number (and hence cavity length) where the re-entrant jet dominates, thus producing a single dominant shedding frequency. At lower cavitation numbers, the cavity length becomes so large that re-entrant jet fluid is generally swept downstream and only occasionally reaches the forming sheet to initiate breakup.

4. Conclusions

Cavitating flows, although complex, permit the use of direct visualization to investigate various flow phenomena. Low- and high-speed photography were used to investigate cavitation occurrence about a sphere and gain insight into the physics of nucleation, coherent shedding and interfacial flow phenomena. The high spatial resolution of low-speed photography permitted the visualization of small-scale structures in the interfacial layer associated with the separating laminar boundary layer and surface tension effects of the detaching cavity. The high temporal resolution of the high-speed photography allowed the study of dynamic phenomena and quantitative data were obtained with the use of numerical processing.

Cavitation about the hydrophilic sphere at a constant Reynolds number of 1.5×10^6 was observed to occur in three modes varying from inception to supercavitation. Inception commenced at a cavitation number around 1.0. Cavity breakup at these high cavitation numbers is due to fine-scale instabilities in the overlying shear layer. Shedding and large-scale cloud formation began with reduction of the cavitation number to around 0.95, where re-entrant jet phenomena started to influence cavity breakup. With further reduction of the cavitation number shedding became more energetic with frequent large-scale events where circumferentially large portions of the cavity were momentarily shed. For cavitation numbers below about 0.4, cavity lengths became sufficient for supercavitation to occur, thereby eliminating the shedding. It is noteworthy that the presence of cavitation allows vortex shedding to occur at a Reynolds number above the limit for this phenomenon in single-phase flow.

Shedding frequencies across the cavitation number range were of the same order as those for low-mode shedding in single-phase subcritical flow, generally reducing with decrease in the cavitation number. At high cavitation numbers shedding occurred at

a dominant Strouhal number of about 0.28. In the shedding mode at intermediate cavitation numbers, frequencies were modulated by the magnitude of shedding events and the connectedness of shed and growing cavities, such that there were two dominant frequencies or a broad spectral peak. Shedding at a single dominant frequency returned at cavitation number of 0.5, where the influence of the re-entrant jet was largely axisymmetric.

Complex interactions between the separating laminar boundary layer and the detaching cavity were observed for all cavitation numbers. In all cases the cavity leading edge was structured in laminar cells separated by so-called divots. These cells were destabilized by K–H instability in the overlying shear layer, resulting in rapid transition to turbulence. In addition to these fine-scale spanwise instabilities, streamwise streaks of similar scale could also be seen on the cavity surface consistent with secondary flow mechanisms observed in single-phase plane mixing layers.

In the shedding mode, the streamwise position of the cavity leading edge exhibited considerable dynamic variation dependent on the magnitude of shedding events. Excursions as large as $\pm 8^\circ$ from the forward stagnation point were observed at a cavitation number of 0.8 where shedding was most energetic. An increase in the initial laminar length of the cavity leading edge and reduced intensity of downstream turbulence showed there to be a general decrease in instability of the interfacial layer with reduction of the cavitation number. In the shedding mode stability conditions were periodically modulated with accelerations and decelerations in the bulk flow. The laminar length was seen to increase during accelerating growth phases and decrease during collapse phases. Divot circumferential density was also observed to vary with local shedding, with divot numbers decreasing during cavity growth phases and increasing during collapse phases.

Where large-scale coherent events occurred with large portions of leading edge extinction, re-nucleation was seen to be circumferentially periodic and to consist of stretched streak-like bubbles that subsequently became fleck-like. This streak- and fleck-like nucleation suggested interaction with the laminar–turbulent transition process of the attached boundary layer. The nucleation process was seen to occur regularly at circumferentially preferred locations, and to form the characteristic cellular cavity leading edge structure with sufficient accumulation of vapour. The circumferential divot spacing was commensurate with estimated local Tollmien–Schlichting wavelength, suggesting that three-dimensional viscous instability of the attached boundary layer may significantly influence the developing structure of the cavity leading edge.

Limitations of the data gathered in the present work indicate that higher spatial and temporal resolutions are required to further investigate the fine-scale high-frequency interfacial instabilities. In this study we have discussed the influence of the boundary layer and its condition on cavity nucleation, the growth and formation of interfacial instabilities and cavity breakup. Differing viscous flow regimes are certain to alter this, and future work also needs to investigate the influence of varying Reynolds number.

The authors wish to acknowledge the assistance of Mr Bryce Pearce in carrying out experiments, and the support of the Australian Defence Science and Technology Organisation, Australian Maritime College and University of Tasmania.

REFERENCES

Achenbach, E. 1972 Experiments on the flow past spheres at very high Reynolds numbers. *J. Fluid Mech.* **54** (3), 565–575.

Achenbach, E. 1974 Vortex shedding from spheres. *J. Fluid Mech.* **62** (2), 209–221.

Addison, P. S. 2002 *The Illustrated Wavelet Transform Handbook*. Taylor and Francis.

Arakeri, V. H. 1975 Viscous effects on the position of cavitation separation from smooth bodies. *J. Fluid Mech.* **68** (4), 779–799.

Arakeri, V. H. & Acosta, A. J. 1973 Viscous effects in the inception of cavitation on axisymmetric bodies. *J. Fluids Engng* **95** (4), 519–527.

Arakeri, V. H. & Acosta, A. J. 1976 Cavitation inception observations on axisymmetric bodies at supercritical Reynolds numbers. *J. Ship Res.* **20** (1), 40–50.

Arndt, R. E. A. 1976 Semi-empirical analysis of cavitation in the wake of a sharp-edged disk. *J. Fluids Engng* **98**, 560–562.

Bakić, V. & Perić, M. 2005 Visualization of flow around sphere for Reynolds numbers between 22 000 and 400 000. *Thermophys. Aeromech.* **12** (3), 307–315.

Belahadji, B., Franc, J. P. & Michel, J. M. 1995 Cavitation in the rotational structures of a turbulent wake. *J. Fluid Mech.* **287**, 383–403.

Brandner, P. A., Clarke, D. B. & Walker, G. J. 2004 Development of a fast response probe for use in a cavitation tunnel. In *15th Australasian Fluid Mechanics Conference*, p. 4. The University of Sydney, Sydney.

Brandner, P. A., Walker, G. J., Niekamp, P. N. & Anderson, B. 2007 An investigation of cloud cavitation about a sphere. In *16th Australasian Fluid Mechanics Conference*, pp. 1392–1998. Crown Plaza, Gold Coast.

Brennen, C. E. 1970*a* Cavity surface wave patterns and general appearance. *J. Fluid Mech.* **44** (1), 33–49.

Brennen, C. E. 1970*b* Some cavitation experiments with dilute polymer solutions. *J. Fluid Mech.* **44** (1), 51–63.

Brennen, C. E. 1995 *Cavitation and Bubble Dynamics*. Oxford University Press.

Briançon-Marjollet, L., Franc, J. P. & Michel, J. M. 1990 Transient bubbles interacting with an attached cavity and the boundary layer. *J. Fluid Mech.* **218**, 355–376.

Ceccio, S. L. & Brennen, C. E. 1992 Dynamics of attached cavities on bodies of revolution. *J. Fluids Engng* **114** (1), 93–99.

Fage, A. 1936 Experiments on a sphere at critical Reynolds numbers. *Reports and Memoranda* 1766. Aeronautical Research Council.

Farge, M. 1992 Wavelet transforms and their applications to turbulence. *Annu. Rev. Fluid Mech.* **24**, 395–457.

Franc, J. P. 2001 Partial cavity instabilities and re-entrant jet. In *Fourth International Symposium on Cavitation*. California Institute of Technology, Pasadena, CA.

Franc, J. P. & Michel, J. M. 2004 *Fundamentals of Cavitation*. Kluwer.

Hinze, J. O. 1955 Fundamentals of the hydrodynamic mechanism of splitting in dispersion processes. *AIChE J.* **1** (3), 289–295.

Ho, C.-M. & Huerre, P. 1984 Perturbed free shear layers. *Annu. Rev. Fluid Mech.* **16**, 365–422.

Jaffard, S., Meyer, Y. & Ryan, R. D. 2001 *Wavelets: Tools for Science and Technology*. SIAM.

Joseph, D. D. 1998 Cavitation and the state of stress in a flowing liquid. *J. Fluid Mech.* **366**, 367–378.

Kjeldsen, M. & Arndt, R. E. A. 2001 Joint time frequency analysis techniques: a study of transitional dynamics in sheet/cloud cavitation. In *Fourth International Symposium on Cavitation* (ed. C. E. Brennen, R. E. A. Arndt & S. L. Ceccio). California Institute of Technology, Pasadena, CA.

Li, C.-Y. & Ceccio, S. L. 1996 Interaction of single travelling bubbles with the boundary layer and attached cavitation. *J. Fluid Mech.* **322**, 329–353.

Mørch, K. A., Bark, G., Grekula, M., Jøenck, K., Nielsen, P. L. & Stendys, P. 2003 The formation of cavity clusters at sheet cavity/re-entrant jet contact. In *Fifth International Symposium on Cavitation*, pp. GS–4–005. Osaka, Japan.

Padrino, J. C., Joseph, D. D., Funada, T., Wang, J. & Sirignano, W.A. 2007 Stress-induced cavitation for the streaming motion of a viscous liquid past a sphere. *J. Fluid Mech.* **578**, 381–411.

Reisman, G. E., Wang, Y. C. & Brennen, C. E. 1998 Observations of shock waves in cloud cavitation. *J. Fluid Mech.* **355**, 255–283.

Schmidt, S. J., Sezal, I. H., Schnerr, G. H. & Thalhamer, M. 2008 Numerical analysis of shock dynamics for detection of erosion sensitive areas in complex 3-D flows. In *WIMRC Cavitation Forum 2008*, pp. 107–120. Warwick, UK.

Schnerr, G. H., Schmidt, S., Sezal, I. & Thalhamer, M. 2006 Shock and wave dynamics of compressible liquid flows with special emphasis on unsteady load on hydrofoils and on cavitation in injection nozzles. In *Sixth International Symposium on Cavitation*. Maritime Research Institute, Wageningen, The Netherlands.

Tassin Leger, A., Bernal, L. P. & Ceccio, S. L. 1998 Examination of the flow near the leading edge of attached cavitation. Part 2. Incipient breakdown of two-dimensional and axisymmetric cavities. *J. Fluid Mech.* **376**, 91–113.

Tassin Leger, A. & Ceccio, S. L. 1998 Examination of the flow near the leading edge of attached cavitation. Part 1. Detachment of two-dimensional and axisymmetric cavities. *J. Fluid Mech.* **376**, 61–90.

Torrence, C. & Compo, G. P. 1998 A practical guide to wavelet analysis. *Bull. Am. Met. Soc.* **79** (1), 61–78.

Van den Braembussche, R., (Ed.) 2002 *Lecture Series on Supercavitation, RTO-EN-010 AC/323(AVT-058)TP/45*. Von Karman Institute for Fluid Dynamics, Sint-Genesius-Rode, Belgium.